RESEARCH ARTICLE

THE PROTEIN SOCIETY   WILEY

Understanding the stability of a plastic-degrading Rieske iron oxidoreductase system

Jessica Lusty Beech[1] [ORCID] | Anjani K. Maurya[2] | Ronivaldo Rodrigues da Silva[1] |
Emmanuel Akpoto[1] | Arun Asundi[2] | Julia Ann Fecko[3] |
Neela H. Yennawar[3] | Ritimukta Sarangi[2] | Christopher Tassone[2] |
Thomas M. Weiss[2] | Jennifer L. DuBois[1]

[1]Department of Chemistry and Biochemistry, Montana State University, Bozeman, Montana, USA

[2]Stanford Synchrotron Radiation Lightsource, SLAC National Accelerator Laboratory, Menlo Park, California, USA

[3]The Huck Institutes of the Life Sciences, The Pennsylvania State University, University Park, State College, Pennsylvania, USA

Correspondence
Jennifer L. DuBois, Department of Chemistry and Biochemistry, Montana State University, Bozeman, MT 59717, USA.
Email: jennifer.dubois1@montana.edu

Abstract

Rieske oxygenases (ROs) are a diverse metalloenzyme class with growing potential in bioconversion and synthetic applications. We postulated that ROs are nonetheless underutilized because they are unstable. Terephthalate dioxygenase (TPA$_{DO}$ PDB ID 7Q05) is a structurally characterized heterohexameric $\alpha_3\beta_3$ RO that, with its cognate reductase (TPA$_{RED}$), catalyzes the first intracellular step of bacterial polyethylene terephthalate plastic bioconversion. Here, we showed that the heterologously expressed TPA$_{DO}$/TPA$_{RED}$ system exhibits only ~300 total turnovers at its optimal pH and temperature. We investigated the thermal stability of the system and the unfolding pathway of TPA$_{DO}$ through a combination of biochemical and biophysical approaches. The system's activity is thermally limited by a melting temperature (T_m) of 39.9°C for the monomeric TPA$_{RED}$, while the independent T_m of TPA$_{DO}$ is 50.8°C. Differential scanning calorimetry revealed a two-step thermal decomposition pathway for TPA$_{DO}$ with T_m values of 47.6 and 58.0°C ($\Delta H = 210$ and 509 kcal mol^{-1}, respectively) for each step. Temperature-dependent small-angle x-ray scattering and dynamic light scattering both detected heat-induced dissociation of TPA$_{DO}$ subunits at 53.8°C, followed by higher-temperature loss of tertiary structure that coincided with protein aggregation. The computed enthalpies of dissociation for the monomer interfaces were most congruent with a decomposition pathway initiated by β-β interface dissociation, a pattern predicted to be widespread in ROs. As a strategy for enhancing TPA$_{DO}$

Reviewing Editor: Lynn Kamerlin

stability, we propose prioritizing the re-engineering of the β subunit interfaces, with subsequent targeted improvements of the subunits.

1 | INTRODUCTION

Enzymes offer the possibility of green solutions to many urgent societal needs. As catalysts, enzymes are characterized by their astonishing rate enhancements ($\leq 10^{12}$-fold), exceptional substrate and reaction specificity, high yields, a preference for aqueous solvents and low temperatures, renewable and non-toxic production, and seemingly endless adaptability through directed evolution and protein engineering. Yet, the promise of these molecules has not been fully realized, in part because of the intrinsic thermal instability of their structures.

Stability is an emergent property depending on many levels of protein structure, any of which could limit the functional lifetime of the enzyme. Functionally significant substructures include active sites and substrate channels, protein–protein interaction surfaces, and subunit interfaces, in addition to the tertiary and secondary structures of individual enzyme subunits. Low stability may be adaptive in the native cellular context where protein motions or binding of proteins to ligands may depend on structural flexibility. However, instability can also limit enzymes' functional lifetime and consequently their biotechnological value.

Directed evolution and computational approaches have successfully stabilized enzymes from several classes, bringing them into the biotechnological toolbox. Results for some monomeric and/or cofactor-free proteins that lack quaternary structure have been impressive (Ao et al., 2023; Calvo-Tusell et al., 2023; Kim et al., 2016; Kunzendorf et al., 2023; Reetz, 2013; Roda et al., 2023; Tournier et al., 2020; Zhang et al., 2023). Many complex, multicomponent metalloenzyme families, however, have no representative in commercial catalogs. The same enzymes have also not been widely adopted for metabolic engineering applications despite their potential value and years of research aimed at understanding their mechanisms. The multi-protein, multi-cofactor nature of complex enzymes presents intrinsic challenges for protein engineering, and the native enzymes themselves may be insufficiently robust for direct use.

The Rieske oxygenases (ROs) are multimeric α_3 or $\alpha_3\beta_3$ enzymes that depend on an active site mononuclear non-heme iron and a *bis*-histidyl, *bis*-cysteinyl coordinated "Rieske" Fe_2S_2 cluster. These cofactors bridge the interface between the α subunits and constitute the site of reactions between substrates and O_2. ROs interact with an accompanying reductase that accepts an NAD(P)H-derived hydride at a flavin adenine dinucleotide (FAD) or mononucleotide (FMN) cofactor. The reductase delivers electrons one at a time to the oxygenase via Fe_2S_2 clusters that are housed within the reductase and/or an accompanying ferredoxin protein (Cosper et al., 2002; Ferraro et al., 2005; Kincannon et al., 2022; Li et al., 2020). The β subunits do not contain catalytic cofactors and their roles have not been explicitly clarified in every RO subtype; however, a binding site for ferredoxin that spans the α and β subunits has been identified (Tsai et al., 2022), and the β subunits appear to have an important role in maintaining ferredoxin affinity. Functionally, ROs resemble the heme-dependent cytochrome P450 enzymes (P450s), which have been adopted in at least some in vitro and metabolic engineering applications (Hobisch et al., 2021; Hollingsworth & Poulos, 2015; Li et al., 2020; Poulost et al., 1987; Serioukova et al., 1999; Tripathi et al., 2013). Like P450s, ROs may catalyze the insertion of one oxygen atom into a substrate (monooxygenation) or simple 2-electron oxidations (Guengerich, 2018). Unlike P450s, they also catalyze a wide range of two oxygen atom insertions (dioxygenations) on natural and non-natural aromatic substrates.

The Rieske dioxygenases are consequently valuable targets for use in green chemical applications involving aromatic molecules (Brimberry et al., 2023). Bacterial assimilation of polyethylene terephthalate (PET) plastic, a copolymer of aromatic terephthalate (TPA) and ethylene glycol, depends on a RO/reductase pair for TPA catabolism. Terephthalic acid dioxygenase (TPA_{DO}) isolated from *Comamonas* strain E6, a soil bacterium with an optimum growth temperature of 30°C, is an $\alpha_3\beta_3$ RO with a catalytic mononuclear Fe at the tail end of each of its comma-shaped, α subunits (each 48.1 kDa), approximately 12 Å from a Rieske cluster at the adjacent subunit's head (Figure 1). Its triad of β subunits (each 17.2 kDa) is cofactor-free. The role of the β subunits are further hypothesized to complete the docking area for the
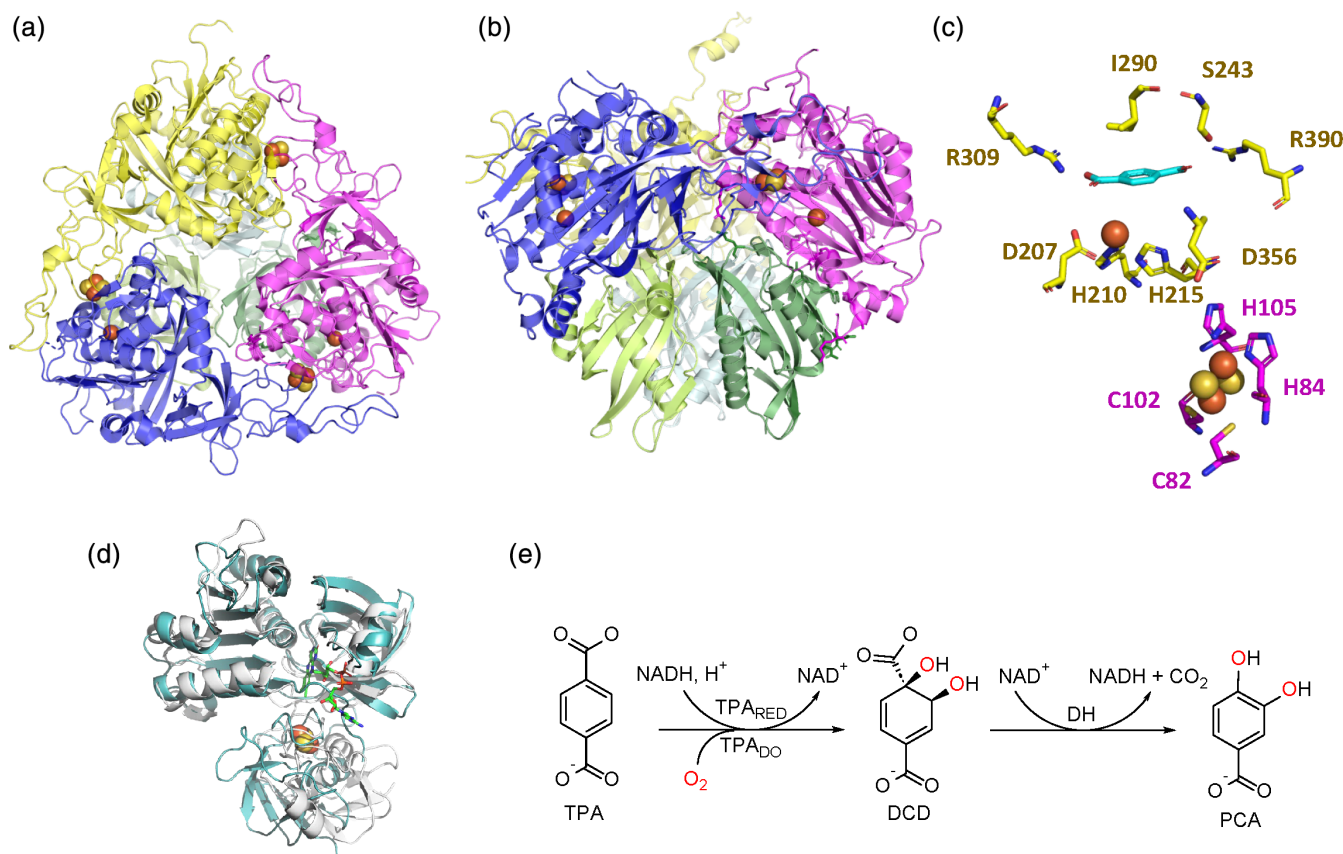
FIGURE 1 The structure of and reaction catalyzed by TPA_DO (PDB ID 7Q05). (a) Top-down view along the enzyme's molecular C_3 axis shows the catalytic trimer of α subunits, each of which contains a Rieske iron sulfur cluster and a mononuclear non-heme iron (spheres: iron = rust; sulfur = yellow). (b) The $β_3$ trimer (subunits in varying shades of green) lies directly below the $α_3$ trimer, shown here in a side-on view parallel to the C_3 axis. (c) Active site residues and cofactors are shown with carbons colored as in (a). Additionally: oxygen = red, nitrogen = blue, and sulfur = yellow. TPA is shown in cyan. (d) An AlphaFold (Jumper et al., 2021; Varadi et al., 2022) generated structure of cofactor-free TPA_RED (blue) is shown overlayed with 4WQM (Acheson et al., 2015), a toluene 4-monooxygenase reductase with the highest sequence similarity to TPA_RED (28% sequence similarity). Cofactors FAD (sticks) and plant-type FeS cluster (spheres) from 4WQM are shown. All structure figures were produced using Pymol. (e) Scheme showing reactions catalyzed by TPA_RED, TPA_DO, and DH.

electron transport proteins and potentially aid in electron transfer despite lacking cofactors or conserved active site residues (Tsai et al., 2022). Along with its cognate FAD/Fe_2S_2-dependent reductase (TPA_RED), TPA_DO catalyzes the stereo- and regioselective conversion of NADH, O_2, and TPA to NAD^+ and the *cis*-dihydroxylation product: 1,2-dihydroxy-3,5-cyclohexadiene-1,4-dicarboxylate (DCD) (Fukuhara et al., 2008; Kincannon et al., 2022). A dehydrogenase (DH) from the same operon oxidatively re-aromatizes DCD, producing protocatechuic acid (PCA) while regenerating NADH. PCA can be completely metabolized by many bacteria or used as a substrate in metabolic pathways that have been engineered to produce valuable chemicals (Alejandro-Marín et al., 2014; Clarkson et al., 2017; Contzen & Stolz, 2000; Dagley et al., 1968; Jamaluddin et al., 1970; Philipp et al., 2002; Sasoh et al., 2006; Walsh & Ballou, 1982; Yun et al., 2004). Bacterial species have an abundance of

homologous 3-enzyme cascades capable of metabolizing major lignin-derived compounds, naphthalene, steroids, and a wide variety of other aromatic substances (Fetherolf et al., 2020; Gibson & Parales, 2000; Kamimura et al., 2017; Kauppi et al., 1997; Kokkonen et al., 2021; Morawski et al., 2000; Neidle et al., 1991; Takahashi et al., 2014; Takahashi et al., 2018; Tavakoli et al., 2016; Tsang et al., 1996; Wei et al., 2014).

Understanding the stability of native ROs is crucial for developing protein engineering strategies to optimize their performance. In this study, we demonstrated that the total turnover number (TTN) for the TPA_DO/TPA_RED system was approximately ~300 molecules of TPA per TPA_DO active site. This observation confirmed our expectation that the native enzyme is not sufficiently stable for biotechnological use. We subsequently aimed to link the loss of function with structural changes in TPA_DO, with the ultimate goal of tailoring engineering strategies to

address specific structural weaknesses. To that end, we correlated functional and thermodynamic stability measured by differential scanning calorimetry (DSC) with a description of thermally-driven, solution-state changes in the TPA_{DO} structure using a combination of light scattering and spectroscopic approaches. Our findings identified substructures near the β-subunit interfaces that are most vulnerable to thermal disruption and therefore constitute primary targets for re-engineering.

2 | RESULTS

TPA dioxygenation under optimal conditions was limited to roughly 300 turnovers per dioxygenase active site. TPA_{RED} and TPA_{DO} were expressed, purified, and analyzed for purity and cofactor content as previously described, (Kincannon et al., 2022) resulting in protein yields of 2.0 mg and 0.70 mg g^{-1} of wet cell paste, respectively (48 and 13 mg L^{-1} of culture). Typical results are shown in Figure S1. Atomic absorption (AA) and UV/visible absorbance (UV/vis) analyses indicated close to stoichiometric cofactor incorporation (Figure S2). Averaging results for three purifications yielded: TPA_{DO}, 7.9 ± 0.5 equivalents of iron per protein; TPA_{RED}, 1.7 ± 0.08 equivalents of iron and 0.95 ± 0.08 of flavin adenine dinucleotide (FAD). Size exclusion chromatography (SEC) confirmed the expected subunit composition, molecular weight, and purity of each enzyme (data not shown).

The optimal steady state ratio of TPA_{RED}:TPA_{DO} was then determined by measuring activity as a function of increasing molar ratio of TPA_{RED} to TPA_{DO}, resulting in a value of approximately three TPA_{RED} to one TPA_{DO} (one TPA_{RED} per TPA_{DO} active site) (Figure S3). A stoichiometric relationship between these active sites indicates that electron transfer from the reductase to the oxygenase reaches a saturating rate without the need for excess reductase. Apparent K_M values for NADH and TPA were subsequently measured for the system with 3:1 TPA_{RED}:TPA_{DO} in ambient air, which reflects a functionally relevant but potentially sub-saturating O_2 concentration yielding K_M(NADH) = 15.8 μM, K_M(TPA) = 40.8 μM, and k_{cat}(TPA) = 23.6 min^{-1} (Figure S3). All kinetic quantities are reported per-TPA_{DO} active site, assuming 3 active sites per TPA_{DO}, throughout this work.

The approximate catalytic lifetime of the TPA_{DO}/TPA_{RED} system was estimated by continuously monitoring consumption of NADH over time via UV/vis absorbance spectroscopy (UV/vis, Figure S4). The total turnover number (TTN) for the TPA_{DO}/ TPA_{RED} system was then quantified over a similar time interval by
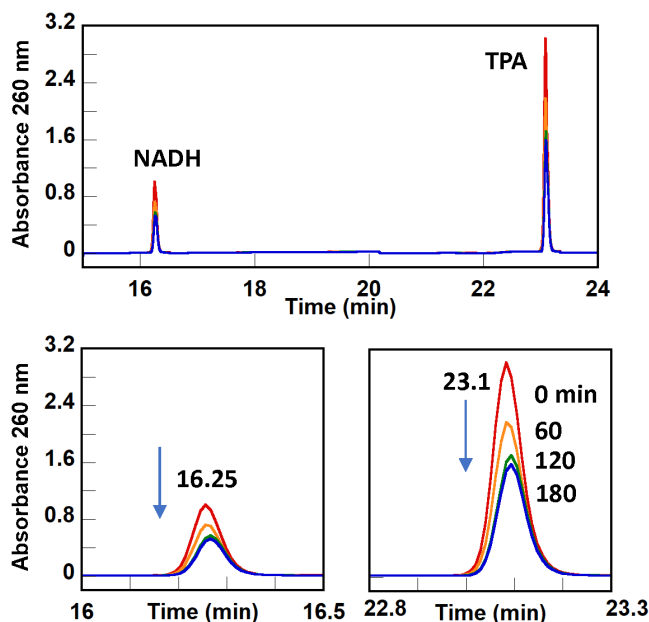
FIGURE 2 A total turnover number of approximately 300 molecules of TPA per TPA_{DO} active site was determined for the TPA_{DO}/TPA_{RED} system using HPLC. (Top) HPLC traces with peaks due to NADH (16.4 min retention time) and TPA (23.3 min) were measured every 10 min for 180 min. Data are shown for t = 0 (red), 60 (orange), 120 (green), and 180 (blue) min. (Bottom) Peaks showing consumption of NADH (left) and TPA (right) over time are shown on a larger scale. Conditions used were: 1 mM TPA, 1 mM NADH, 1.9 μM TPA_{DO}, 5.7 μM TPA_{RED} in 20 mM MOPS pH 7.2, 150 mM NaCl, 20% v:v DMSO, 28°C.

discontinuously measuring consumption of TPA and NADH via high-performance liquid chromatography (HPLC) peak integration relative to standard curves (Figure 2). TPA and NADH substrates were added in increments until no additional NADH consumption was observable (Kincannon et al., 2022). TTN per TPA_{DO} active site was: 310 ± 23 (continuous UV/vis) or 260 ± 55 (HPLC) for NADH, and 250 ± 43 for TPA (HPLC). The values for NADH consumption were the same within error whether measured by continuous or discontinuous methods. Moreover, NADH and TPA were consumed in an approximately 1:1 ratio. This suggested that the TPA_{DO}/TPA_{RED} system effectively coupled NADH consumption to TPA dihydroxylation under the conditions used, without significant generation of H_2O_2 as a side product. The overall TTN was nonetheless low compared to values measured for P450 oxygenases, which can range from 1000 to 50,000 (Hobisch et al., 2021). TTN was also low relative to values commonly targeted for biocatalysis applications, though TTN benchmarks can vary widely depending on the enzymes themselves and the process in which they are to be used (Bommarius, 2015; Dias Gomes & Woodley, 2019).
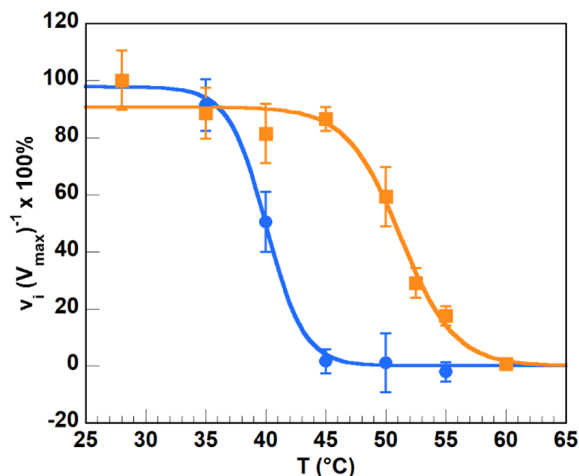
FIGURE 3 Temperature tolerance of TPA$_{DO}$ (orange) and [TPA$_{DO}$ + TPA$_{RED}$] (blue) were evaluated by incubating the enzyme pair or TPA$_{DO}$ alone at a series of elevated temperatures for 20 min, equilibrating the enzyme system to 28°C, and measuring their activity via continuous monitoring of NADH absorbance. Measured activities were referenced to V_{max}, a value obtained when both enzymes were maintained at the control temperature (28°C) throughout the equilibration period. Data points are the average of at least 3 measurements, and error bars represent ±1 standard deviation. The data were fitted to a reverse sigmoidal curve. (See Methods.) T_m is equal to the temperature at which $v_i/V_{max} = 50\%$. The two-enzyme system was limited overall by the thermotolerance of TPA$_{RED}$. Conditions used were: 100 μM TPA, 200 μM NADH, 1.9 μM TPA$_{DO}$, 5.7 μM TPA$_{RED}$ in 20 mM MOPS pH 7.2, 150 mM NaCl, 20% v:v DMSO.

TPA$_{DO}$ activity (v_i) was lost with $T_m = 50.8$°C. The thermal stability of TPA$_{DO}$/ TPA$_{RED}$ activity, where the enzymes were used in a 1:3 ratio and at saturating concentrations of NADH and TPA, was determined by incubating both enzymes at a series of increasing temperatures for 20 min. After heating, the enzymes were re-equilibrated to their functional optimum of 28°C where $v_i = V_{max}$ (Kincannon et al., 2022). The enzymes were then mixed and their residual activity assayed by measuring the decrease in NADH absorbance (340 nm) over time (100 μM TPA, 200 μM NADH, 1.9 μM TPA$_{DO}$, 5.7 μM TPA$_{RED}$ in 20 mM MOPS pH 7.2, 150 mM NaCl, 20% v:v DMSO). Activities were referenced to the value of V_{max} measured when the enzymes were incubated at the control temperature (28°C). The data fit well to a reverse sigmoid curve, indicating a dose–response relationship between v_i/V_{max} and temperature. Loss of activity began at 35°C, with a midpoint temperature (T_m) of 39.9°C (Figure 3).

We reasoned that activity could be limited either by the thermal stability of TPA$_{DO}$ or TPA$_{RED}$. In order to independently assess the thermal stability of TPA$_{DO}$ function, the experiment was repeated in exactly the same
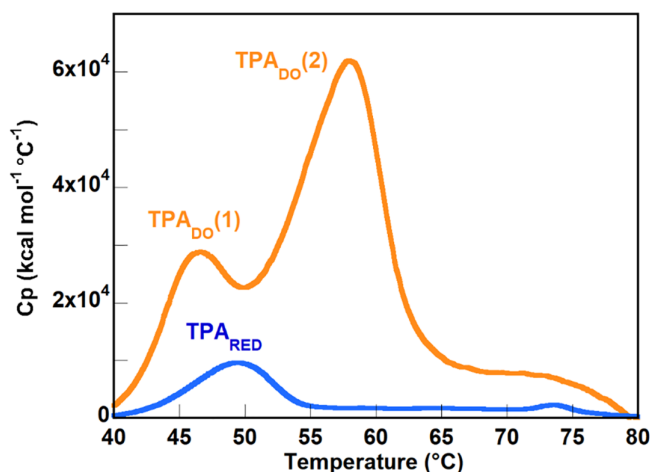
FIGURE 4 DSC profiles identified a two-phase thermal dissociation pathway for TPA$_{DO}$ (orange) and a single-phase pathway for TPA$_{RED}$ (blue). Representative data are shown. See Table 1 for T_m and ΔH values determined from the average of three independent measurements.

fashion; however, only TPA$_{DO}$ was heated, while TPA$_{RED}$ was incubated in each case at 28°C. The heated TPA$_{DO}$ was re-equilibrated to 28°C prior to mixing with TPA$_{RED}$ and carrying out the activity assay. The system retained full activity above 45°C, with a T_m of 50.8°C (Figure 3). Because the TPA$_{DO}$ active site consists of iron cofactors deriving from the head (mononuclear Fe) and tail (Rieske cluster) of adjacent α subunits, we reasoned that at least an intact α$_3$ structure and the iron ions would be required for full activity. Whether the β subunits would be necessary for retaining TPA$_{DO}$ activity was unknown prior to this investigation. Our attempts to heterologously express the α subunits alone resulted in no soluble protein or enzymatic activity (data not shown). The thermodynamic limits on the active forms of the enzymes were further investigated.

Thermal dissociation of TPA$_{DO}$ occurred via two successive and partially overlapping transitions, while TPA$_{RED}$ unfolded in a single step. TPA$_{RED}$ and TPA$_{DO}$ were examined via capillary DSC. This method monitors the heat absorbed (q) by a sample of molecules maintained at a constant pressure as a function of increasing temperature. Data were plotted as the constant-pressure molar heat capacity (Cp) versus temperature, where Cp is equal to q/T and $\Delta H/T$. The temperature at which each structural transition occurred was determined by fitting the midpoint of the peak, and ΔH was determined from the peak area.

A DSC profile for a multi-subunit protein can consist of a single peak, in which quaternary and tertiary structures are disrupted in a concerted, cooperative manner. Alternatively, multiple peaks indicate stepwise,

TABLE 1 Thermal unfolding transitions observed for TPA$_{DO}$, TPA$_{RED}$, and the TPA$_{DO}$–TPA$_{RED}$ complex.

	T_m (1) (°C)	ΔH (1) (kcal mol^{-1})	T_m (2) (°C)	ΔH (2) (kcal mol^{-1})	T_m (3) (°C)	ΔH (3) (kcal mol^{-1})
TPA$_{DO}$	47.6 ($\pm$0.45)	210 ($\pm$12)	58.0 ($\pm$0.26)	509 ($\pm$16)	72.4 ($\pm$0.50)	71 ($\pm$11)
TPA$_{RED}$	48.4 ($\pm$0.054)	79.8 ($\pm$4.1)	71.6 ($\pm$1.2)	14 ($\pm$3.2)		

Note: 20 mM Tris, pH 8, 150 mM NaCl, 10% v:v glycerol [TPA$_{DO}$] = 0.5 mg mL^{-1}; 20 mM Tris, pH 8, 300 mM NaCl, 15% v:v glycerol [TPA$_{RED}$] = 0.5 mg mL^{-1}.

non-cooperative unfolding (Carvalho et al., 2012). Because TPA$_{DO}$ is an oligomer with distinct α-α, α-β, and β-β subunit interfaces, we reasoned that subunit dissociation could either precede or coincide with the loss of the α and β tertiary and/or secondary structures, depending on the relative free energy associated with each transition and the mechanism of thermal denaturation. Moreover, if the subunits dissociate partially from one another prior to losing their tertiary structures, they could separate to yield one or more semi-stable intermediates. See for example the variety of thermally available quaternary structures assumed by insulin in the presence of zinc (Carpenter & Wilcox, 2014; Lisi et al., 2014).

Heat flow to purified TPA$_{DO}$ was monitored as temperatures were ramped from 30°C to 80°C. The DSC trace revealed two transitions with T_m 47.6°C (ΔH = 210 kcal mol^{-1}) and 58.0°C (ΔH = 509 kcal mol^{-1}), based on the average of three independent measurements. (See Figure 4 for representative plots and Table 1 for averaged parameters.) The presence of two, partially overlapping DSC transitions indicated that TPA$_{DO}$ unfolded in a non-cooperative manner, suggesting an unfolding intermediate (Table 1). The first transition occurred with roughly the same T_m observed in the plot of fractional activity versus temperature for TPA$_{DO}$ (50.8°C, Figure 3). This suggested that activity loss was associated with the lower temperature structural transition.

By contrast, DSC analysis of the much smaller (37 kDa) monomeric TPA$_{RED}$ identified one well-defined transition with T_m = 48.4°C (ΔH = 79.8 kcal mol^{-1}). Interestingly, this T_m was well above the midpoint temperature associated with activity loss by TPA$_{RED}$ (39.9°C, Figure 3). This implies that the activity loss associated with TPA$_{RED}$ was likely thermally regulated by factors other than the structural transitions observable by DSC. These could include active site structural rearrangements that disfavor catalysis, dissociation of the Fe$_2$S$_2$ cofactor from the protein, or localized unfolding around the protein surface where TPA$_{RED}$ interfaces with TPA$_{DO}$. These hypotheses will be addressed in future work focusing specifically on RO reductases.

Finally, an additional small shoulder with T_m = 71–72°C was observed for both enzymes, after which the

DSC traces curved toward the baseline. These high-temperature peaks were attributed to loss of all residual folded substructures.

TPA$_{DO}$ secondary structure loss occurred gradually, with α-helical content sensitive to thermal denaturation even at low T. The thermal decomposition of TPA$_{DO}$ secondary structure was monitored using circular dichroism (CD) spectra measured as a function of temperature. CD provides a composite estimate of a protein's α-helicity and β-sheet content (Greenfield, 2006). The TPA$_{DO}$ spectrum was measured first at 25°C, for which the BeStSel server (Micsonai et al., 2018) predicted 10.2% helix (32% expected) and 27.2% sheet (31% expected), with the remaining structure consisting of loops and turns. Spectra were then measured at 1°C increments from 40 to 60°C to gauge the thermal stability of each type of secondary structure (Figure 5a). We observed a gradual decrease in CD signal with temperature across this temperature range, with no discrete T_m. The helical content observable in the room temperature CD spectrum was more heat sensitive than the β-sheets and was mostly eliminated even before the first step of thermal dissociation observed by DSC (T_m = 47.6°C). By contrast, CD indicated that significant β-sheet secondary structure was maintained beyond the first unfolding event and up to 50°C. Most of the α-helices in the TPA$_{DO}$ crystal structure are solvent exposed, with the notable exception of one 20-residue long N-terminal helix at the β$_3$ interface and three helices that shape the active site (Figure 5c). Loss of α-helix content at low temperatures suggested that the active site iron cofactors may be particularly susceptible to dissociation from the α$_3$β$_3$ complex (Micsonai et al., 2015; Micsonai et al., 2018).

The initial unfolding event observed by DSC corresponded to structural elongation in the β$_3$ unit, consistent with SAXS data. Purified TPA$_{DO}$ was initially characterized by small angle x-ray scattering on protein eluting from an in-line size exclusion column (SEC-SAXS) to investigate the solution phase native structure of the protein. SEC-SAXS data (Table S3) demonstrated that TPA$_{DO}$ possessed a compact and globular structure with a radius of gyration (Rg) of 38.2 Å and a molecular weight of ~194 kDa (Figure S5). The SEC-SAXS data
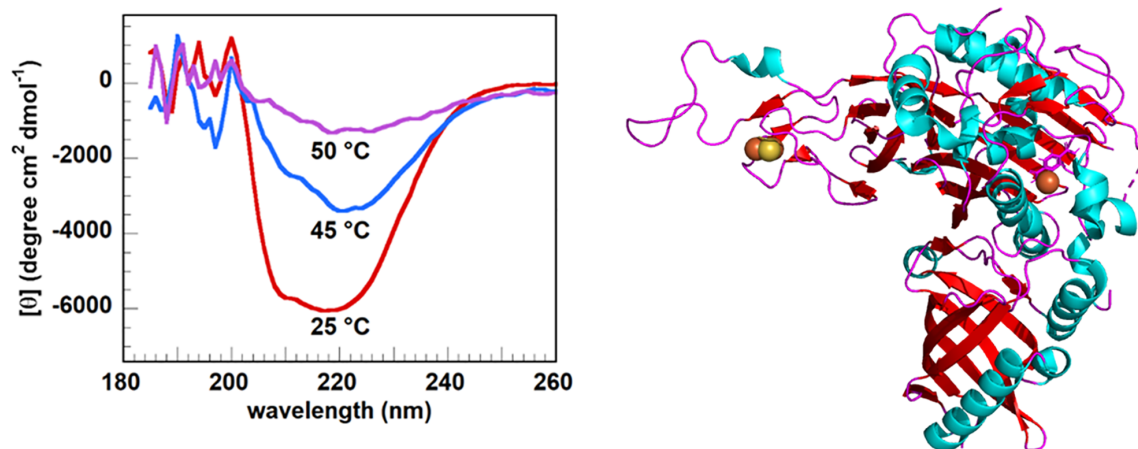
FIGURE 5 Circular dichroism spectroscopy data illustrating the temperature-dependent loss of secondary structure for TPA_DO. Left: The protein was allowed to equilibrate to increasing temperatures at 1°C increments, after which CD spectra were measured. Data are plotted at selected temperatures here. A gradual loss of secondary structure was observed above 40°C. The trough near 220 nm reflects the retention of some β-sheet structure at 50°C. Right: Secondary structural elements for a single α/β pair and their interface, viewed perpendicular to the protein's C_3 axis with the cofactor-containing α subunit at the top and the β subunit at the bottom.
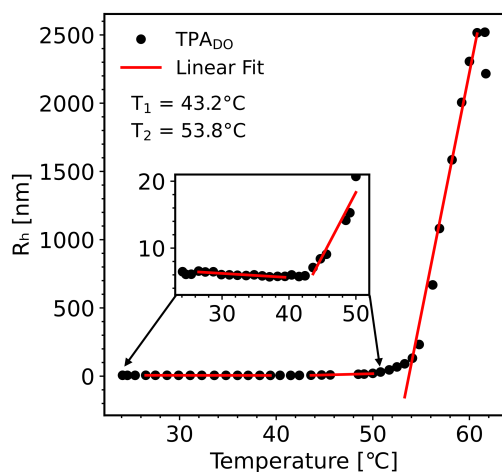
FIGURE 6 Temperature-dependent SAXS measurements of TPA_DO indicated changes in the solution structure with added heat. (a) Indirect Fourier transform fit using the GNOM package from ATSAS provided an estimate of the I_0, R_g, $P(r)$, and maximum dimension of the macromolecule (Svergun, 1992). These structural features were used to quantify changes in protein structure as a function of temperature. (b) Extracted pair distance distribution functions ($P(r)$) from SAXS data measured at various temperatures, excluding temperatures at which Guinier regions were not reliably identified. (c) R_g, I_0, and MW are plotted as a function of temperature.
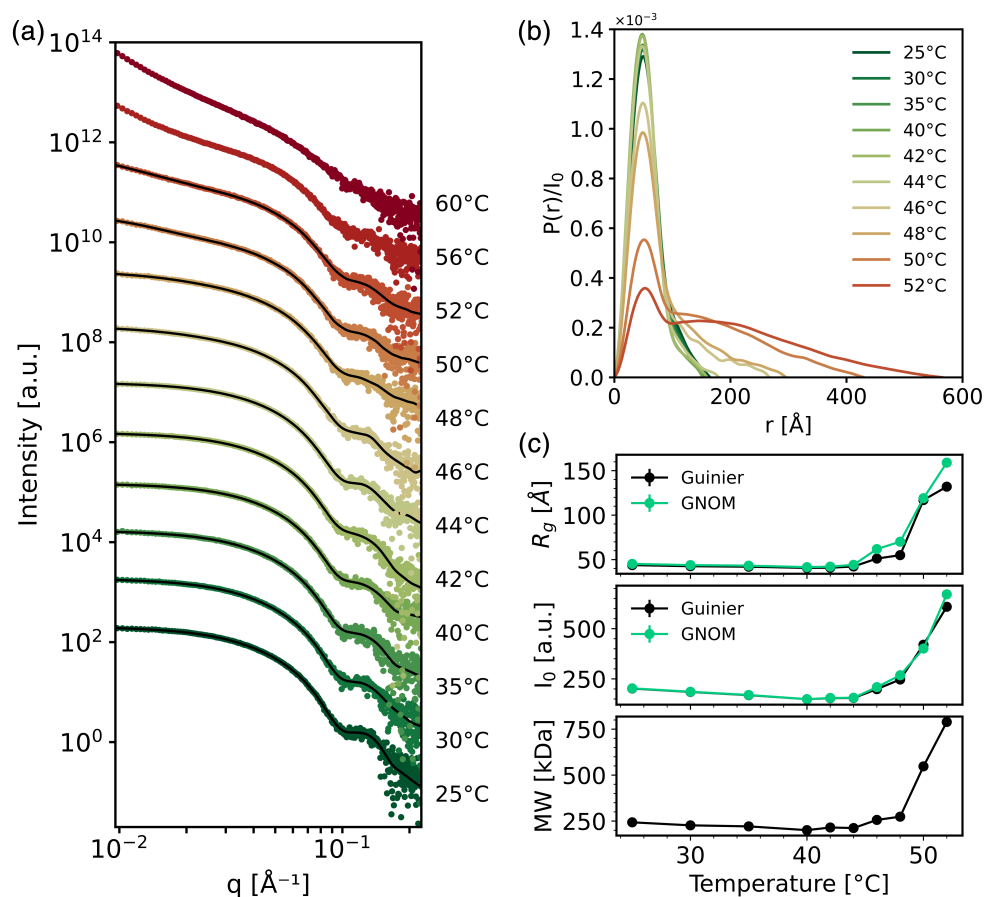
were well fit with the high-resolution structure of TPA_DO. The SEC traces from TPA_DO show two shoulders bookending the major $\alpha_3\beta_3$ species peak corresponding to the minor presence of aggregated or subunit-dissociated states. The well-fit SEC-SAXS data, however, suggests

that the major species present preserved the crystallographic $\alpha_3\beta_3$ structure.

We then used temperature-dependent SAXS to investigate structural changes around the transition temperatures identified by DSC and CD. To ensure both

FIGURE 7 Temperature-dependent dynamic light scattering (DLS) measurements identified the onset of two distinct transitions. T_1 and T_2 were determined as the intersections of linear fits within three distinct hydrodynamic radius (R_h) regions, as marked by the fitted red lines. The inset plot provides a close-up look at the R_h versus temperature graph associated with the onset of the first transition at T_1.

temperature stability and to prevent radiation damage during SAXS measurements, the protein samples were incubated for 60 s at temperature intervals between 25 and 60°C, while using different sample aliquots in an overlapping manner for each temperature point. The SAXS profiles obtained at different temperatures (Figure 6a) were initially analyzed using an indirect Fourier transform (IFT) fitting approach with the GNOM package (Svergun, 1992). Fits were overlaid on the measured data up to 52°C. The corresponding pair-distance distribution function ($P(r)$), R_g, and the forward scattering intensity at zero angle (I_0) are provided in Figure 6b, c. R_g and I_0 values were also determined independently using the Guinier fit, and molecular weights were calculated using an adjusted Porod volume method (Figure 6c) (Fischer et al., 2010). Both data fitting procedures gave identical values. Complete measurement details and fitted parameters are summarized in Tables S4 and S5.

In the temperature-dependent SAXS experiments starting at 25°C, we observed an initial slight reduction in Rg, I_0, and MW with increasing temperature up to 42°C. These changes were likely associated with the dissociation of bound subunits that previously formed incomplete oligomers, which were suggested to be present in the sample by the shoulder in the SEC-SAXS profile (Figure S5). From 42 to 52°C, we noted a gradual increase in R_g, I_0, and MW, accompanied by a notable elongation in the normalized $P(r)$ function that may be due to the elongation in the protein shape. Elongation would lead to exposure of hydrophobic surfaces to water,

and non-specific aggregation of the complex. A pronounced upturn in the SAXS profile was evident at temperatures of 56 and 60°C, consistent with accelerated protein aggregation due to the added heat. Consequently, IFT and Guinier fits could not be reliably performed at these elevated temperatures.

To complement the investigation of TPA$_{DO}$'s thermal response by SAXS, we used dynamic light scattering (DLS) measurements, which monitor the dynamic behavior of the protein particles using non-ionizing, visible light. Figure 7 shows a plot of the DLS-derived hydrodynamic radius (R_h) as a function of temperature (correlation functions given in Figure S6). We identified three regions with different, approximately linear temperature dependencies separated by two distinct onset transition points, T_1 and T_2. These were identified as the intersection points of linear fits to the three regions of the R_h versus temperature plot (Figure 7; Table S6). We observed a decrease in R_h across the first region (25.0–43.2°C), followed by a gradual increase in R_h up to 53.8°C. Beyond this temperature, there was a rapid upsurge in R_h. T_1 and T_2 coincided with the transition points observed by SAXS and the onset temperature corresponded to the first and second transitions observed by DSC. This provided further strong evidence that the changes observed in the SAXS measurements are inherent to the TPA$_{DO}$ molecule's structural response to temperature and were not a consequence of x-ray radiation damage.

The mononuclear Fe site is highly labile. The function of TPA$_{DO}$ depends on three iron ions coming respectively from a Rieske-type Fe$_2$S$_2$ cluster and a mononuclear non-heme iron center in adjacent α subunits (Figure 1). We examined the relative lability of these iron species at 25°C via their susceptibility to chelation by ethylenediaminetetracetic acid (EDTA).

Atomic absorption spectroscopy was used to determine total iron content per protein before and after dialysis against 5 mM EDTA, a strong chelator which should remove any weakly associated iron species. Prior to treatment with EDTA, the newly purified TPA$_{DO}$ sample contained 9.0 ($\pm$0.9) equivalents of iron per protein. Afterward, this number dropped to 4.1 ($\pm$0.6). UV/vis absorbance spectra of the pre- and post-dialysis protein indicated that the characteristic Fe$_2$S$_2$ cluster spectrum was mostly retained, suggesting the mononuclear Fe ions might have been removed (data not shown). Weak binding of the mononuclear Fe, which is nestled in an active site surrounded by α-helices (Figure 5), is consistent with the T-dependent CD analysis, which indicated the low-temperature loss of α-helical structures.

The available crystal structures are also consistent with weak mononuclear Fe binding (Kincannon

et al., 2022). In the substrate-free state (PDB ID 7Q04), the mononuclear Fe was modeled in a highly distorted 2-coordinate geometry and was observed at only one of the three TPA$_{DO}$ active sites (Figure S7). In the TPA-bound and 2-hydroxy-TPA bound structures (PDB IDs 7Q05 and 7Q06), the observed coordination numbers increased to 3 and 4, respectively, and a portion of α-helix at the boundary of the active site rotated toward the metal. We speculate that the weakly bound mononuclear Fe dissociated from the protein during crystallization of the substrate-free protein, and that substrate binding partially stabilized the otherwise flexible activate site structure.

X-ray absorption spectroscopy (XAS) was used to investigate the structures of the TPA$_{DO}$ iron centers in solution. As-isolated and post-dialysis proteins were concentrated to an iron concentration of 2 mM. The Fe K-edge XAS data of the as-isolated protein is expected to exhibit a weighted average of 1/3 non-heme Fe-like features and 2/3 Rieske Fe-like features (Cho et al., 2011; Cosper et al., 2002; Hermes et al., 2006; Sarangi et al., 2008; Schmitt & An, 2017; Tsang et al., 1989). A loss of non-heme Fe occupancy in the post-dialysis protein is expected to result in an increased average in pre-edge intensity and decrease in maximum absorption based on published data on non-heme and Rieske Fe XAS. However, the Fe K-edge spectra (Figure S8A) for both the as-isolated and post-dialysis proteins showed pre-edge and maximum absorption intensities that strongly resembled the spectral signatures typical of Rieske Fe sites (Cosper et al., 2002; Tsang et al., 1989), suggesting low occupancy of the mononuclear Fe sites with or without treatment of the protein with chelators. The spectrum did not change upon introduction of TPA to the as-isolated protein, consistent with low Fe occupancy of the non-heme Fe sites where substrate is expected to bind.

Deconvolution of the pre-edge feature showed no change in intensity and only a slight decrease in energy for the post-dialysis protein, consistent with the lack of structural change between these samples (Figure S9, Table S7). The extended x-ray absorption fine structure (EXAFS) data were well-modeled using scattering paths from Rieske Fe only (1 Fe-N, 3 Fe-S, 1 Fe-Fe) (Figure S10). The fitted structural parameters were consistent with previously reported bond distances for Rieske-type proteins (Cosper et al., 2002; Link, 1999; Tsang et al., 1989) and showed no differences for all samples within the uncertainty of the model (Figures S9B, S11, and Table S8). Attempts to include scattering contributions from a potential non-heme Fe site worsened the quality of the fits.

Together these results strongly indicate that the non-heme Fe site in TPA$_{DO}$ is labile. We propose that concentrating the protein for XAS measurement (at 4°C) depleted most or all of the non-heme Fe sites via the law of mass action, even without the use of chelators or input of thermal energy. However, loss of catalytic activity is correlated with the initial thermal transition observed via DSC and described structurally by T-SAXS. This suggests that as long as the protein's architecture remains intact, the mononuclear Fe may be able to dissociate from and rebind at the active site. The lability of the mononuclear iron has been well documented with other ROs, with reports of systems requiring supplemental iron to restore maximum activity due to iron loss during purification (Bernhardt & Meisch, 1980; Correll et al., 1992; Suen & Gibson, 1993; Wolfe et al., 2002; Wolfe & Lipscomb, 2003) and may be dependent upon the oxidation state of the iron center (Ohta et al., 2008). The absence of mononuclear iron signal in TPA$_{DO}$ after robust handling in preparation for XAS analysis supports the canonical understanding of this weakness of RO systems.

2.1 | Predictions based on informatics and structural analyses

EMBL PISAePDB was developed as a tool for predicting solution-state protein assemblies based on x-ray crystallographic structures. It identifies noncovalent interactions within/between protein subunits and uses these to propose both the strength of interaction between and dissociation pathways for the monomers composing protein oligomers (Evgeny Krissinel, 2003; Krissinel & Henrick, 2007; Krissneil & Henrick, 2005). Four features are summarized: numbers of hydrogen bonds (H-bonds), salt bridges, cysteine cross links, and buried surface area that is solvent-protected by inter-subunit associations. These together contribute to the enthalpy of subunit dissociation for a particular subunit-subunit interface ($\Delta H_{dissociation}$). We analyzed the TPA-bound TPA$_{DO}$ structure (PDB ID 7Q05) using EMBL PISAePDB (https://www.ebi.ac.uk/msd-srv/prot_int/pistart.html) to enumerate structural features promoting the stability of its quaternary and tertiary structures (Evgeny Krissinel, 2003; Krissneil & Henrick, 2005). The free energies of dissociation and solvation for protein oligomers are challenging to model with accuracy; hence, the discussion of PISAePDB outputs here is structure-driven and qualitative.

PISAePDB predicted that the crystallographically observed α$_3$β$_3$ TPA$_{DO}$ is the thermodynamically preferred

TABLE 2 Structural features of TPA$_{DO}$ subunit interfaces summarized by PISAePDB.

	TPA$_{DO}$ (*Comamonas* E6, PDB ID 7Q05)			Average values for 12 homologous αβ ROs			Naphthalene dioxygenase (*Rhodococcus* sp. NCIMB 12038, PDB ID 2B1X)		
	α–α	β–β	α–β	α–α	β–β	α–β	α–α	β–β	α–β
H-bonds	6	3	21	24	18	28	28	16	28
Salt bridges	7	6	11	11	8	13	10	7	14
Interface area (Å^2)	1258	587	1510	1620	1281	1704	1552	1118	1750

Note: See Table S1 for complete PISAePDB output and further information on the set of enzymes included in the averages. There were no intersubunit cysteine disulfides identified via crystallographic structure determination in any of the proteins described in this study.

oligomeric state in solution. This was corroborated here by SEC-SAXS and prior size exclusion chromatography (Figure S5, Table S3) (Kincannon et al., 2022). The heterohexamer was predicted to be ~40 kcal mol^{-1} more stable than the next-most-stable structure, an α$_3$-only TPA$_{DO}$ assembly. The stability of the α$_3$ unit was similar in magnitude to that computed for ROs that naturally lack β subunits and are α-homotrimers, such as phthalate dioxygenase (Figure S14) (Mahto et al., 2021). The predicted moderate stability of the TPA$_{DO}$ α$_3$ assembly reflects the small number of β-β subunit interactions relative to the α-β and α-α interfaces (Table 2). Accordingly, PISAePDB also predicted an α$_3$ + 3β dissociation pathway for TPA$_{DO}$ ($\Delta H_{dissociation} = 109$ kcal mol^{-1}, Table S1). We note that this pathway is broadly consistent with the DSC-measured $\Delta H = 210$ kcal mol^{-1} associated with the first DSC transition (Figure 4, Table 1) and the much larger ΔH associated with the second DSC transition. We attribute the latter to cooperative dissociation of the α$_3$ unit and loss of tertiary structures from the α and β subunits.

To put the PISA predictions into the context of other structurally characterized ROs, the structure of TPA$_{DO}$ was used as a query for EMBL PDBeFold (https://www.ebi.ac.uk/msd-srv/ssm), which identified several similar, empirically determined structures of homologous proteins in the Protein Data Bank (Krissinel & Henrick, 2004). Results were sorted by secondary structure elements, and structures with ≥40% similarity to TPA$_{DO}$ were compiled. The resulting set included 12 αβ ROs, one of which (the naphthalene dioxygenase from *Rhodococcus* sp. strain NCIMB12038, PDB ID 2B1X) was previously shown to be thermostable via temperature-dependent CD spectroscopy up to 95°C (Gakhar et al., 2005). In addition, six α-only ROs were identified, of which five had α$_3$ and one had an α$_6$ oligomerization state (full results in Tables S1 and S2, Figure S14). In every case, the predicted solution phase oligomerization state was also the one that was crystallographically observed. Other than the *Rhodococcus* enzyme above, for which CD spectra but not activity were monitored, we were unable to identify melting temperatures or other literature data relevant to the thermal stability of the enzymes. None derived from a known thermophilic organism.

Each structure was analyzed by EMBL PISAePDB, and the full list of PISA-generated parameters was examined to identify any trends. First, an α$_3$ + 3β deoligomerization pathway was predicted for 11 of the 12 heterohexamers, with one α$_3$ + β$_3$ dissociation. We noted that the average $\Delta H_{dissociation}$ for the α$_3$β$_3$ heterohexamers was about twice that for the α-only enzymes (including the α$_6$ structure), similar to the predicted relationship between the α$_3$β$_3$ and a hypothetical α$_3$-only TPA$_{DO}$. The β$_3$ unit, which does not contain any catalytically essential cofactors, clearly contributes substantially to the thermal stability of the α$_3$β$_3$ oligomer. Second, the one experimentally documented thermostable RO from the list (naphthalene dioxygenase, PDB ID 2B1X) was predicted to have the highest overall $\Delta H_{dissociation}$ and $\Delta G_{dissociation}$, consistent with the complex's expected stability. This observation provided some qualitative validation for the PISAePDB output. Finally, when comparing the α$_3$β$_3$ ROs to one another, no *single* structural parameter appeared to correlate strongly with either the predicted $\Delta H_{dissociation}$ or $\Delta G_{dissociation}$. For example, TPA$_{DO}$ had the smallest β-β surface area among all of the structurally characterized α$_3$β$_3$ ROs. However, neither the predicted $\Delta G_{dissociation}$ for this interface nor for TPA$_{DO}$ as a whole was exceptionally small (Table S1). The small surface area was not compensated by a large number of H-bonds or salt bridges, compared with the average numbers of noncovalent linkages for the α$_3$β$_3$ ROs, or for the thermally stable structure 2B1X. Moreover, no single structural parameter appeared to point toward 2B1X as a thermostable protein, either on its own, when compared with others in the set, or when compared to the averaged parameters for the entire list of α$_3$β$_3$ ROs. However, the β-β interface of TPA$_{DO}$ was markedly smaller and had several fewer noncovalent interactions than either 2B1X or the average α$_3$β$_3$ enzyme, suggesting that it is a particularly weak interface.

3 | DISCUSSION

Discovery, evolution, and engineering approaches have elevated the status of many enzymes from being merely interesting to becoming useful in practice. However, other enzyme families, including the RO/reductases, remain largely outside of the biotechnological toolbox. These enzyme systems have not been widely adopted as a class in either in vitro or synthetic biology applications, despite their potential value for important applications including plastic and lignin bioconversion (Clarkson et al., 2017; Fetherolf et al., 2020; Kamimura et al., 2017; Kincannon et al., 2022; Kontur et al., 2019; Takahashi et al., 2014). We hypothesized that a limited functional lifetime may be a key barrier preventing these enzymes from being used.

We consequently examined the stability of the plastic-converting TPA$_{DO}$ enzyme from *Comamonas* strain E6, measuring its catalytic lifetime and probing its thermal dissociation trajectory via complementary thermodynamic and structural approaches. The results revealed a remarkably fragile TPA$_{DO}$/TPA$_{RED}$ system that completed only 300 turnovers of TPA before irreversibly inactivating, even at the temperature determined to be optimal for its activity (Figure 2). Following incubation at increasing temperatures, the TPA$_{DO}$ complex lost all catalytic activity with a T_m at 50.8°C, which is likely not suitably thermostable for several applications including downstream bioconversion of PET near its glass transition temperature (Yoshida et al., 2016). We correlated activity loss with a thermal transition observable by DSC at roughly the same temperature ($T_m = 47.6°C$, $\Delta H = 210$ kcal mol^{-1}, Table 1), which we ascribed to dissociation of the $\alpha_3\beta_3$ subunits. In support of this model, the SAXS-determined solution-phase structure also underwent a thermal transition beginning at 42°C in which the TPA$_{DO}$ radius of gyration expanded, consistent with changes in the quaternary structure (Figure 6, Table S5). Enthalpic arguments based on the TPA$_{DO}$ structure (PISAePDB) suggested that the weakly associated β subunits become detached from one another and ultimately from the α_3 unit with added heat. A second, higher temperature and higher enthalpy transition was observed by DSC ($T_m = 58°C$) (Figure 4). The same temperature range was marked by a pronounced expansion in the SAXS profile and a significant increase in R_h observed by DLS, consistent with loss of tertiary structure followed by protein aggregation.

Protein stability results from many small, additive, contributing factors. The structural and thermodynamic description of TPA$_{DO}$ presented here highlights the importance of the subunit interfaces in stabilizing the enzyme's structure as a whole. Subunit dissociation, either partial or complete, occurred as a discrete step observable by DSC (Figure 4). The stabilities of TPA$_{DO}$ and other structurally characterized $\alpha_3\beta_3$ ROs, while impossible to predict with accuracy, are reflected in the relative values of $\Delta G_{dissociation}$ (and $\Delta H_{dissociation}$) computed by PISAePDB, which were far more endergonic (and endothermic) in $\alpha_3\beta_3$ ROs than for α_3 ROs (Table S1). This suggests that the β subunits via both β-β and α-β interfaces contribute substantively to RO stability.

Analysis of these interfaces among TPA$_{DO}$ and its structurally characterized homologs is instructive. TPA$_{DO}$ (PDB ID 7Q05) contains four salt bridges and two hydrogen bonds in each β-β interface. These noncovalent interactions, however, are exclusively located between one pair of residues, D142 and R80 (Figure S11). Conversely, the β-β interface of the structure of a thermotolerant RO (PDB ID 2B1X), has 10 salt bridges from three unique pairs of residues and 21 hydrogen bonds spread among 18 unique residue pairs (Table S9). This comparison suggests that engineering stability into interfaces along the β_3 triad could provide a strategy for improving the stability of TPA$_{DO}$ and possibly $\alpha_3\beta_3$ ROs more broadly. Interestingly, the PISAePDB dissociation model for most $\alpha_3\beta_3$ ROs predicts an initial dissociation of β subunits from each other and the α_3 trimer. The β-β interface has the added advantage of being set apart from functionally significant parts of the enzyme, including the active site and potential docking sites for TPA$_{RED}$. Engineering at the β interfaces may benefit from an expansion of not only the overall number of noncovalent interactions, but in the number and spacing of bonded residue pairs. The α-β interface is also apparently weaker in TPA$_{DO}$ than in the homologous structures, though the β-β interface is by far the weakest surface within the TPA$_{DO}$ quaternary structure (Tables 2 and S1). The α-β interface may also partially overlap with the surface where TPA$_{DO}$ and TPA$_{RED}$ dock, though the site of protein–protein interaction in this RO system remains to be determined.

In addition to the subunit structure, TPA$_{DO}$ is expected to possess some degree of instability near its two cofactors. Peptide flexibility near the iron centers is clearly necessary for maintaining catalytic function. The iron sites need to accommodate the substrate entry/product release, oxidation-state-dependent changes in bond lengths and hydrogen bonding interactions, and particularly dramatic rearrangements in the coordination environment at the mononumclear iron (Figure S15). Extensive prior work with related ROs has shown that substrate binding displaces a water molecule from the fully reduced active site, opening a coordination position on the mononuclear Fe(II) for O$_2$. The coordination state of the mononuclear iron then shifts from square

pyramidal to trigonal bipyramidal. (Baratto et al., 2019; Ohta et al., 2008; Wolfe et al., 2002; Wolfe & Lipscomb, 2003), resulting in a more tightly bound metal. We noted a greater susceptibility toward chelation of the mononuclear Fe versus the Rieske cofactor (Figures S9 and S10). The mononuclear iron can likely reversibly bind to the TPA$_{DO}$ active site, since activity remains intact until the temperature at which subunit interactions are interrupted is reached (Figure 3). The Rieske cluster remains protein-associated despite being bound within a collection of flexible loops that could have permitted its departure from the protein (Figure 5). The head-to-tail orientation of the α subunits results in the Rieske domain overlapping with an α-helix of the adjoining subunit (residues 353–367) that is located proximal to the protein core. This arrangement may shield the Rieske cluster against dissociation without compromising flexibility that may be critical for catalysis. Conversely, the mononuclear non-heme iron coordinates two histidine residues, H210 and H215, and D356 in a bidentate mode in a portion of the α subunit with a well-defined secondary structure (α-helices). The crystal structures of substrate-bound and substrate-free TPA$_{DO}$ (Figure S7) reveal a rotation in the stretch of α-helix containing both H210 and H215, as well as shifts in the positions of the coordinating residues that allow them to bind to the iron after TPA binds. These changes in coordination and the structural flexibility they imply appear to be necessary for catalysis (Kincannon et al., 2022). Hence, preserving activity in this RO system demands a balance between flexibility in the structure and retention of the active oligomeric state.

4 | CONCLUSIONS

We observed that TPA$_{DO}$ is a remarkably fragile enzyme, with its chief thermal limitations at the quaternary level and likely focused at the β-β interfaces. Though the inclusion of the β$_3$ triad is not essential for catalysis, it adds significantly to the overall predicted stability of the enzyme provided that it remains intact. Future work will build on these findings using computationally-guided redesign.

5 | MATERIALS AND METHODS

5.1 | Protein expression

Genes encoding the TPA oxygenase alpha subunit (tphA2, BAE47077), beta subunit (tphA3, BAE47078) and TPA reductase (TPA$_{RED}$) (tphA1, BAE47080) were synthesized in pET-Duet and pET45b expression vectors,

respectively, by GenScript. Lemo21(DE3) *E. coli* cells (New England Biolabs) harboring the pETDuet-TPA$_{DO}$ or pET45b-TPA$_{RED}$ constructs were grown overnight from a glycerol stock at 37°C in 50 mL LB media (5 g sodium chloride, 5 g yeast extract, 10 g tryptone per 1 L MilliQ water) and used to inoculate 500 mL Terrific Broth in 2.8 L Fernbach flasks (1:100 v:v dilution). The medium was supplemented with ampicillin (0.050 mg mL^{-1}), chloramphenicol (0.034 mg mL^{-1}), and rhamnose (2 mM). Cultures were grown at 37°C, 225 rpm on an Innova shaker incubator until the optical density (OD$_{600nm}$) >2.5 (5–6 h). Flasks were cooled by complete submersion in ice for 45 min. The ice-chilled cultures were supplemented with 0.1 mM ferric chloride and 10 mg/L L-cysteine hydrochloride monohydrate. The TPA$_{RED}$ cultures were further supplemented with 0.2 mg mL^{-1} (−)-riboflavin. Protein production was induced with 1 mM (TPA$_{DO}$) or 0.4 mM (TPA$_{RED}$) isopropyl β-D-1-thiogalactopyranoside (IPTG). Flasks were incubated at 25°C, 200 RPM for 18 h, then cells were harvested via centrifugation at 4°C. Cell paste was frozen in liquid N$_2$ and stored at −80°C.

5.2 | Protein purification

Proteins were purified by immobilized metal (Ni^{2+}) affinity chromatography. TPA$_{DO}$ cell pellets were resuspended in buffer A (20 mM TrisHCl, 150 mM NaCl, 10% glycerol v:v%, pH 8.0), with approximately 30 g cell paste to 200 mL of buffer. The protease inhibitor phenylmethylsulfonyl fluoride (PMSF) and chicken egg white lysozyme were added to 1 mM and 1 mg mL^{-1}, respectively. Solutions were incubated at room temperature with stirring for 15 min to initiate lysis followed by sonication (Branson) on ice: 25 min, with a pulse sequence of 10 s on and 25 s off, at 40% amplitude. Lysates were clarified via centrifugation (18,000 × g, 30 min, 4°C). Supernatants were loaded onto a 20 mL Ni^{2+} charged nitrilotriacetic acid (MCLAB) affinity column pre-equilibrated in buffer A. The column was washed with 200 mL buffer A then 600 mL 60% buffer A and 40% buffer B (buffer A with 0.25 M imidazole). Proteins were eluted with 100% buffer B and pure fractions (≥95% assessed by SDS-PAGE) were concentrated approximately 10-fold to a final volume of 5 mL using a 30 MWCO using Amicon centrifugal filtration devices and desalted into buffer A using a PD-10 column (BioRad), reconcentrated to a final concentration close to 10 mg mL^{-1}, aliquoted, and flash frozen in liquid N$_2$ before storing at −80°C until use.

TPA$_{RED}$ cell pellets were resuspended in buffer C (20 mM TrisHCl, 300 mM NaCl, 15% glycerol v:v%, pH 8.0), with 20 g cell paste in 160 mL of buffer. Cells

were lysed as described above. Clarified lysate was loaded onto a 20 mL Ni^{2+} charged nitrilotriacetic acid (MCLAB) affinity column, washed with 600 mL buffer C, and eluted via mixtures of buffer C and buffer D (buffer C with 250 mM imidazole). Proteins were eluted at 5%–50% buffer D. Pure proteins were pooled and concentrated with 10 MWCO Amicon centrifugal filtration devices, desalted into buffer C using a PD-10 column (BioRad), concentrated, and stored as above.

5.3 | Protein analyses

Protein concentrations were routinely measured via the Bradford assay (Noble, 2014). Iron-containing cofactors were quantified per protein using AA spectroscopy, assuming that 9 atoms are needed per TPA$_{DO}$ holoprotein and 2 per TPA$_{RED}$. Iron quantitation was completed using a SpectrAA 220 Fast Sequential Atomic Absorption Spectrometer (Varian, Palo Alto, CA, USA) An iron AA standard (Ricca, 1000 ppm in 3% HCl) was used to generate a calibration curve by creating standards ranging from 1 to 72 μM. P TPA$_{DO}$ samples were diluted to 0.7–2.5 μM protein (∼6–23 μM Fe). TPA$_{RED}$ samples were diluted to 1–5 μM protein (∼2–10 μM Fe). To prevent damage to the instrument due to protein presence, protein samples were inoculated with 500 μL of a 30% nitric acid solution, boiled at 100°C for 5 min, then filtered through a 0.22 μM filter to remove bulk precipitated protein particulates. The resulting clarified samples were then analyzed (Figure S2). A regression analysis of the linear curve fit to each protein sample determined an error of 0.5 for the slope of TPA$_{DO}$ and 0.08 for the slope of TPA$_{RED}$ (Figure S2).

FAD was quantified using UV–Visible spectroscopy. TPA$_{RED}$ was diluted to 11, 15, and 20 μM in triplicate. Full spectra (280–700 nm) scans were taken for each concentration. FAD was released from TPA$_{RED}$ by denaturing 200 μL of diluted protein solution with 50 μL saturated ammonium sulfate, 7% v:v H$_2$SO$_4$, similar to studies with related cytochrome P450s (Swoboda, 1969). Precipitated protein was pelleted by centrifugation and the UV–Visible spectrum of the FAD-containing supernatant was measured from 280 to 700 nm. The absorbance at 450 nm, $\varepsilon_{FAD} = 11.1$ mM^{-1} cm^{-1} (Macheroux, 1999), and total protein concentrations were used to determine [FAD] bound to TPA$_{RED}$. The concentration of acid-extracted flavin was then used to calculate the extinction coefficient for flavin in the TPA$_{RED}$ protein (16.13 mM^{-1} cm^{-1}). Both free and protein bound flavin concentrations were plotted against TPA$_{RED}$ concentrations and fit with a straight line with standard deviation represented by error bars. A regression analysis of the linear curve fit determined an error of 0.081 for the slope (Figure S2).

5.4 | Quantification of substrate turnover HPLC

The TTN of the system (number of TPA molecules oxidized per TPA$_{DO}$ active site) was measured at 28°C. 2 mL reactions in quartz cuvettes contained TPA$_{DO}$ (1.9 μM active site) and TPA reductase (5.7 μM active site) in 20% v:v DMSO, 150 mM NaCl, 20 mM MOPS pH 7.2. To initiate the reaction, 25 μL each TPA and NADH from 1.6 mM stocks (final concentration 200 μM each) were added to the cuvettes, which were aerated periodically by pipette aspiration. Samples were withdrawn every 5 min for 180 min, quenched with ice-cold methanol, and analyzed for NADH and TPA concentration by HPLC with a Shimadzu instrument with a diode array detector and Thermo Scientific™ Hypersil GOLD™ (4.6 mm × 250 mm, 5 μm particle size) column. The column was pre-equilibrated in 95% buffer A and 0% buffer B. Buffer A consisted of 0.1% (v/v) TFA (Fisher) in water. Buffer B consisted of 0.1% (v/v) TFA (Fisher) in HPLC grade acetonitrile (Fisher). The reaction components were eluted at a rate of 1 mL min^{-1} with the following program: 5% B from 0.0 to 10.0 min, 0 to 15% B from 10.0 to 18.0 min, 15 to 75% B from 18.0 to 24.0 min, 75 to 100% B from 24.0 to 24.1 min, 100% B from 24.1 to 30.1 min, 100% to 0% B from 30.1 to 30.2 min, and 0% B from 30.2 to 38.0 min. NADH (Alfa Aesar) and TPA (Sigma-Aldrich), were used to generate standard curves via integration of peaks monitored at the 240 nm and retention times of 16.25 and 23.1 min, respectively. The reaction endpoint was confirmed by addition of fresh substrates which remained unconverted into products.

5.5 | Steady state kinetics

Initial rates of reaction were measured using a Thermo Varioskan spectrophotometer 96 well plate reader, recording absorbance changes due to NADH at 340 nm ($\varepsilon = 6.22$ mM^{-1} cm^{-1}, [Wood, 1987]) under ambient air (∼250 μM O$_2$) at 28°C in 250 μL volume wells. TPA$_{DO}$ (1.9 μM active site) and TPA$_{RED}$ (variable concentrations) were first diluted from a stock concentration in storage Tris buffer to 20 mM MOPS pH 7.2. Enzymes were added to a reaction buffer which contained final volumes 200 μM NADH, 20% v:v DMSO, 150 mM NaCl in 20 mM MOPS pH 7.2 Reactions were initiated by addition of 25 μL TPA from a 1 mM stock (final concentration = 100 μM). Rates of reactions were

determined from the slope of a line fit by linear regression to the initial 60 s of the time course.

Rates were measured as a function of variable reductase concentration (0.45–13.3 µM active site) in order to determine the optimal ratio of TPA_{RED}: TPA_{DO} and fit to a Langmuir isotherm (Figure S3) using Kaleidagraph. For all further reported kinetic measurements, a $5 \times K$ ratio (fitted $K = 0.63 \pm 0.09$ µM) was used to approximate a saturating concentration of TPA_{RED}, resulting in a working concentration of 1.9 µM active site TPA_{DO} and 5.7 µM active site TPA_{RED}. We then determined k_{cat} and K_M values for NADH and TPA in air referencing the total concentration of TPA_{DO} active site when determining k_{cat}. Because K_{O2} was not known, it is not certain that ambient air results in a saturating concentration of O_2; hence, these values are apparent. [NADH] was varied over 0–300 µM and reactions were initiated by addition of TPA (200 µM) while [TPA_{RED}] was maintained at 5.7 µM. Alternatively, saturating NADH (200 µM NADH) was included in each reaction and [TPA] was varied over 0–1000 µM. Initial rates were plotted as a function of the variable substrate concentration and fit (Kaleidagraph) to the Michaelis–Menten expression (NADH) (Equation 1) or the same expression with a substrate inhibition constant (K_i) included in Equation (2):

$$V_i = \frac{V_{max} \cdot [TPA]}{K_M + [TPA]}. \tag{1}$$

$$V_i = \frac{V_{max} \cdot [TPA]}{K_M + [TPA] \cdot \left(1 + \left(\frac{[TPA]}{K_i}\right)\right)} \tag{2}$$

5.6 | Activity as a function of temperature

To determine the temperature optimum of the TPA_{DO}/ TPA_{RED} system, each enzyme was independently diluted from its stock concentration (20 mM Tris storage buffer) at 86 and 250 µM to 9.5 and 29 µM for TPA_{DO} and TPA_{RED}, respectively in 20 mM MOPS, 150 mM NaCl, pH 8.0. The working enzyme solutions were then aliquoted into separate 200 µL tubes. Each protein tube was incubated either at the target temperature (35, 40, 45, 50, 55, or 60°C) or the control temperature (28°C) in an Eppendorf Mastercycler thermocycler for 20 min, then equilibrated to the reaction temperature (28°C) for 10 min. Following incubation, 50 µL of each enzyme was added to three identical 96-well plate reaction wells containing 125 µL reaction buffer Reactions were initiated by addition of 25 µL TPA from a 2 mM stock (final concentration 200 µM). The final concentrations of the assay were: TPA_{DO} 1.9 µM (intact active site, based on number

of iron equivalents per enzyme by AA) and TPA reductase 5.7 µM (active site, based on AA and FAD, which invariably gave concurrent values), 200 µM NADH, 20% v:v DMSO, 150 mM NaCl in 20 mM MOPS pH 7.2 in air, with <1 mM residual Tris. Reactions were monitored at 28°C in a 96 well plate via UV/Vis absorbance changes at 340 nm due to NADH oxidation (vide supra). Activities (v_i) were reported as micromolar (µM) NADH consumed min^{-1} $µM^{-1}$ TPA_{DO} active site, as a percentage of the activity measured following incubation of both enzymes at the control temperature (28°C) (V_{max}). Measurements were made in triplicate and averaged, and errors were given as ±1 standard deviation. A plot of activity as a function of T was fit to the reverse sigmoidal expression Equation (3). The midpoint of the sigmoid was reported as T_m.

$$\frac{L}{1 + ne^{k \cdot (x - x_0)}}. \tag{3}$$

5.7 | Circular dichroism spectroscopy

Circular dichroism (CD) measurements were performed on a JASCO J-1500 spectrometer, equipped with a Peltier model PTC-517 thermostat cell holder. Temperature interval measurement experiments were run using a range of 40–60°C. The wavelength range scanned was 260–185 nm with a 1°C data interval. Temperature gradient was set to 2°C min^{-1}, pitch to 1.0 nm and a scan speed of 50 nm min^{-1}. Digital integration time was set to 4 s and the bandwidth to 1.0 nm. The quartz cell used had a 1 mm path length. The proteins were prepped as previously described and the final protein concentrations used were 0.5 mg mL^{-1}. Data were analyzed using both the Jasco Spectra Manager software and the online Bestsel server.

5.8 | Differential scanning calorimetry

Differential scanning calorimetry (DSC) measurements were carried out using MicroCal VP-capillary DSC (now Malvern Panalytical). Data were collected over a temperature range of 25–100°C with a scan speed of 90°C h^{-1}. A buffer reference experiment was run to use for baseline subtraction. The cell was loaded with 400 µL of protein at a concentration of 0.5 mg mL^{-1}. The running software was VPViewer2000. The analysis software was Microcal, LLC Cap DSC Version Origin70-L3 which was used to convert the raw data into molar heat capacity (MHC).

5.9 | Size exclusion chromatography SAXS measurement

Size exclusion chromatography coupled small angle x-ray scattering (SEC-SAXS) was performed at beamline 4–2 at the Stanford Synchrotron Radiation Lightsource (SSRL), California, USA. The SEC was performed using a ThermoFisher Scientific UltiMate 3000 UHPLC system, utilizing a Superdex 200 column. The column was equilibrated with a buffer containing 20 mM Tris at pH 8.0 and 150 mM NaCl. Prior to sample injection, the column was pre-equilibrated with the same buffer and 30 μL TPA_{DO} was injected into the column. More details of the SEC-SAXS measurement is given in Table S3. To monitor the eluted protein, absorbance at 280 nm was measured, and the outlet of the SEC system was connected to the Small-angle X-ray scattering (SAXS) setup at the 4–2 beamline. The x-ray beam with dimensions of 300×300 μm² and an energy of 11 keV, along with a Pilatus 1 M detector was used for SAXS measurements. The sample-to-detector distance (SDD) was set at 1.7 m, calibrated using standard silver behenate samples. The protein sample was exposed to the x-ray beam for 1 s to record the scattering pattern continuously. The background scattering was subtracted by referencing a buffer sample.

5.10 | Temperature-dependent SAXS measurement

We conducted SAXS measurements at various temperatures ranging from 25 to 60°C. A temperature-controlled capillary flow cell was employed to ensure precise temperature control during the experiment. To mitigate radiation damage, we utilized fresh aliquots, measuring them in an interleaved manner for each temperature point. Furthermore, the aliquots were oscillated within the measuring capillary to prevent overexposure of the sample at the same position to x-ray radiation. The temperature-dependent SAXS measurements for TPA_{DO} were replicated three times. For each temperature, the sample and buffer were irradiated for 1 s, and a total of 12 frames were recorded. To ensure data quality, any frames showing radiation damage were excluded from the analysis. The remaining frames were then averaged to obtain a representative scattering pattern for the specific temperature. The same SAXS configuration utilized in the SEC-SAXS setup at beamline 4–2 was employed for temperature-dependent measurements as well. This configuration consisted of a beam size of 300×300 μm², an energy of 11 keV, an SDD of 1 m, and a Pilatus 1 M detector.

5.11 | SAXS data reduction and analysis

The collected SEC-SAXS and temperature-dependent SAXS data were initially processed to obtain 1D SAXS profiles using the Blu-Ice program available at beamline 4–2. To eliminate the contribution of buffer scattering, the buffer scattering was subtracted from the enzyme samples. The PRIMUS, a tool from the ATSAS software package, was utilized for determining the radius of gyration (R_g) and forward scattering I0 by Guinier analysis (Manalastas-Cantos et al., 2021). Furthermore, the pair distance distribution function $P_{(r)}$ was obtained through inverse Fourier transformation of the scattering curve using the GNOM package (Svergun, 1992). From the $P(r)$ analysis, the radius of gyration (R_g) and the maximum particle dimension (D_{max}) were determined. CRYSOL package from ATSAS was used for fitting the SEX-SAXS data using high-resolution crystal structure. The Python scripts were used for generating the figures.

5.12 | Temperature-dependent dynamic light scattering measurement

Dynamic light scattering (DLS) measurements were conducted within a temperature range of 25–60°C using a Wyatt Technology DynaPro Plate Reader equipped with a temperature-controlled sample block, allowing for precise temperature monitoring at a rate of 1°C per min. The experimental sample was prepared and loaded into a 96-well plate. To ensure reliable data, 10 frames were captured every 5 s and subsequently averaged to represent each recorded temperature. The acquired DLS data were subjected to analysis using the Wyatt Technology Dynamics software and custom Python scripts. The autocorrelation function was extracted from the raw intensity data, which served as the basis for determining particle size. The particle size was determined through the utilization of the cumulant (ISO 22412 and ASTM 2490-09) and regularization method, a widely accepted technique for size calculations in dynamic light scattering studies.

5.13 | Metal analysis by X-ray absorption spectroscopy

Iron content was quantified for purified protein (As-Isolated) samples by AA as above. Full spectra (200–800 nm) scans were taken from a 1.5 μM TPA_{DO} outlining the characteristic iron sulfur cluster peaks. The sample was then dialyzed in 12 kDa MWCO dialysis tubing (Spectrum Labs, Rockleigh, New Jersey) at 4°C gently stirring for two changes of 1 L (12 h total) in TPA_{DO}

Buffer A with an additional 5 mM EDTA. The next morning, protein was buffer exchanged to remove EDTA using a PD10 column (Cytiva), concentrated using a 10 kDa MWCO Amicon centrifuge concentrator to a final iron concentration 1.9 mM (42 mg mL^{-1} protein). UV–Visible spectra and AA samples were taken for the dialyzed samples following the same procedure as the day prior. Fe K-edge X-ray absorption spectra were collected at the Stanford Synchrotron Radiation Lightsource (SSRL) on the wiggler side-station beam line 9–3 under standard ring conditions of 3 GeV and ~500 mA. Higher harmonics (above ~13 keV) were rejected using a vertically collimating Rh-coated M1 mirror. A liquid N_2-cooled Si(220) double crystal monochromator with crystal orientation $\varphi = 0°$ was used for energy selection. Cuboidal solution cells wrapped with 30 μm Kapton tape were filled with sample solution and flash-frozen in liquid nitrogen. During data collection, samples were held in an Oxford liquid He cryostat and maintained at ~10 K throughout the measurement. Spectra were measured to $k = 16$ Å^{-1} in fluorescence mode. Incident beam intensity was measured with a N_2-filled ionization chamber and fluorescence was measured using a Canberra 100-element liquid N_2-cooled Ge detector selecting the Fe Kα emission line (~6403.8 eV). A 6 μm Mn filter was placed in front of the Ge detector to reduce the signal from the scattered beam. An Fe foil was placed downstream of the sample cryostat and data were recorded using a N_2-filled ionization chamber simultaneously for energy calibration. The first inflection point of the Fe foil spectrum was fixed at 7112 eV.

Data were first processed using SIXPack (Webb, 2005), in which fluorescence channels that exhibited artifacts (e.g., ice diffraction) were removed, and the remaining channels were averaged. For each sample, measuring the same sample spot twice resulted in a slightly red-shifted spectrum, indicating photoreduction of the sample. Therefore, measurements were collected on six different sample spots to ensure replicate spectra were minimally influenced by beam damage. The six replicate spectra were aligned, merged, and energy calibrated in the Athena software of the Demeter package (Ravel & Newville, 2005). Linear pre-edge and post-edge lines were used for baseline subtraction to obtain normalized XAS spectra. XAS pre-edge deconvolution was performed in Matlab using a fixed error function background and series of Gaussian components with varying energies and peak heights. The width of the pre-edge features was also allowed to vary but was constrained to be the same value for all Gaussian components. Pre-edge fits were performed using the fminsearch function in Matlab to minimize the sum of squared residuals between the measured and modeled spectra.

EXAFS background was modeled in the Pyspline program using a three-region spline of orders 2, 3, and 3. EXAFS was modeled using the Artemis program of the Demeter package. Theoretical EXAFS signals $\chi(k)$ were calculated using FEFF6. The EXAFS models were optimized in k-space using k^1, k^2, and k^3-weightings, with the models obeying the Nyquist criterion. EXAFS fits were performed on a k-range of 2–11 Å^{-1} and an R-range of 1–3 Å. The structural parameters varied during the fitting were the bond distance (R) and the bond variance (σ^2). The non-structural global parameter, ΔE_0 (E_0 is the energy at which $k = 0$) was also fit. Coordination numbers were systematically varied over the course of fitting to assess different models but were fixed during a given fit. The value of $S_0{}^2$ was fixed to 0.9 for all fits.

5.14 | Computational structure, interface, and informatics analyses

Similar RO structures were identified by the EMBL eFOLD tool. TPA$_{DO}$ α subunit sequence was input as the query, with results sorted by secondary structure elements. Resulting structures were annotated with substrate and host organism (Table S1). An analysis of the stability of the quaternary structure was conducted using EMBL Proteins, Interfaces, Structures and Assemblies (PDBePISA) tool for TPA$_{DO}$ (PDB ID 7Q05) as well as all structures presented in Table S1 (Evgeny Krissinel, 2003).

AUTHOR CONTRIBUTIONS
Jessica Lusty Beech: Conceptualization; investigation; writing – original draft; methodology; validation; visualization. **Anjani K. Maurya:** Investigation; writing – original draft; writing – review and editing; validation; methodology. **Ronivaldo Rodrigues da Silva:** Investigation; writing – review and editing. **Emmanuel Akpoto:** Investigation; writing – review and editing. **Arun Asundi:** Investigation; writing – original draft; methodology. **Julia Ann Fecko:** Investigation; writing – original draft. **Neela H. Yennawar:** Investigation; writing – review and editing; supervision; resources. **Ritimukta Sarangi:** Supervision; writing – review and editing; funding acquisition. **Christopher Tassone:** Writing – review and editing; supervision; funding acquisition. **Thomas M. Weiss:** Supervision; resources; writing – original draft; investigation. **Jennifer L. DuBois:** Conceptualization; investigation; funding acquisition; writing – original draft; project administration; supervision.

CONFLICT OF INTEREST STATEMENT

The authors declare no conflicts of interest.

ORCID

Jessica Lusty Beech https://orcid.org/0000-0002-4212-6133

REFERENCES

Acheson JF, Moseson H, Fox BG. Structure of t4mof, the toluene 4-monooxygenase ferredoxin oxidoreductase. Biochemistry. 2015;54(38):5980–8.

Alejandro-Marín CM, Bosch R, Nogales B. Comparative genomics of the protocatechuate branch of the β-ketoadipate pathway in the Roseobacter lineage. Mar Genom. 2014;17: 25–33.

Ao YF, Pei SX, Xiang C, Menke MJ, Shen L, Sun CH, et al. Structure- and data-driven protein engineering of transaminases for improving activity and stereoselectivity. Angew Chem Int Ed. 2023;62(23):e202301660.

Baratto MC, Lipscomb DA, Larkin MJ, Basosi R, Allen CCR, Pogni R. Spectroscopic characterisation of the naphthalene dioxygenase from Rhodococcus sp. strain NCIMB12038. Int J Mol Sci. 2019;20(14):3402.

Bernhardt F-H, Meisch H-U. Reactivation studies on putidamonooxin — the monooxygenase of a 4-methoxybenzoate o-demethylase from pseudomonas putida. Biochem Biophys Res Commun. 1980;93(4):1247–53.

Bommarius AS. Biocatalysis: a status report. Ann Rev Chem Biomol Eng. 2015;6:319–45.

Brimberry M, Garcia AA, Liu J, Tian J, Bridwell-Rabb J. Engineering rieske oxygenase activity one piece at a time. Curr Opin Chem Biol. 2023;72:102227.

Calvo-Tusell C, Liu Z, Chen K, Arnold FH, Garcia-Borras M. Reversing the enantioselectivity of enzymatic carbene N-H insertion through mechanism-guided protein engineering. Angew Chem Int Ed. 2023;62(35):e202303879.

Carpenter MC, Wilcox DE. Thermodynamics of formation of the insulin hexamer: metal-stabilized proton-coupled assembly of quaternary structure. Biochemistry. 2014;53(8):1296–301.

Carvalho JW, Santiago PS, Batista T, Salmon CE, Barbosa LR, Itri R, et al. On the temperature stability of extracellular hemoglobin of glossoscolex paulistus, at different oxidation states: SAXS and DLS studies. Biophys Chem. 2012;163-164:44–55.

Cho J, Jeon S, Wilson SA, Liu LV, Kang EA, Braymer JJ, et al. Structure and reactivity of a mononuclear non-haem iron(III)-peroxo complex. Nature. 2011;478(7370):502–5.

Clarkson SM, Giannone RJ, Kridelbaugh DM, Elkins JG, Guss AM, Michener JK. Construction and optimization of a heterologous pathway for protocatechuate catabolism in escherichia coli enables bioconversion of model aromatic compounds. Appl Environ Microbiol. 2017;83(18):e01313-01317.

Contzen M, Stolz A. Characterization of the genes for two protocatechuate 3,4-dioxygenases from the 4-sulfocatechol-degrading bacterium agrobacterium radiobacter strain S2. J Bacteriol. 2000;182:6123–9.

Correll CC, Batiet CJ, Ballou DP, Ludwig ML. Phthalate dioxygenase reductase: a modular structure for electron transfer from pyridine nucleotides to [2Fe-2S]. Science. 1992;258:1604–9.

Cosper NJ, Eby DM, Kounosu A, Kurosawa N, Neidle EL, Kurtz DM Jr, et al. Redox-dependent structural changes in archaeal and bacterial rieske-type [2Fe-2S] clusters. Protein Sci. 2002;11(12):2969–73.

Dagley S, Geary PJ, Wood JM. The metabolism of protocatechuate by *Pseudomonas testosteroni*. Biochem J. 1968;109:559–69.

Dias Gomes M, Woodley JM. Considerations when measuring biocatalyst performance. Molecules. 2019;24(19):3573-3584.

Evgeny Krissinel KH. Inference of macromolecular assemblies from crystaline state. J Mol Biol. 2003;372:774–97.

Ferraro DJ, Gakhar L, Ramaswamy S. Rieske business: structure-function of Rieske non-heme oxygenases. Biochem Biophys Res Commun. 2005;338(1):175–90.

Fetherolf MM, Levy-Booth DJ, Navas LE, Liu J, Grigg JC, Wilson A, et al. Characterization of alkylguaiacol-degrading cytochromes P450 for the biocatalytic valorization of lignin. Proc Natl Acad Sci U S A. 2020;117(41):25771–8.

Fischer H, de Oliveira NM, Napolitano HB, Polikarpov I, Craievich AF. Determination of the molecular weight of proteins in solution from a single small-angle x-ray scattering measurement on a relative scale. J Appl Cryst. 2010;43(1):101–9.

Fukuhara Y, Kasai D, Katayama Y, Fukuda M, Masai E. Enzymatic properties of terephthalate 1,2-dioxygenase of Comamonas sp. strain E6. Biosci Biotechnol Biochem. 2008;72(9):2335–41.

Gakhar L, Malik ZA, Allen CC, Lipscomb DA, Larkin MJ, Ramaswamy S. Structure and increased thermostability of Rhodococcus sp. naphthalene 1,2-dioxygenase. J Bacteriol. 2005; 187(21):7222–31.

Gibson DT, Parales RE. Aromatic hydrocarbon dioxygenases in environmental biotechnology. Curr Opin Biotechnol. 2000;11: 236–43.

Greenfield NJ. Using circular dichroism spectra to estimate protein secondary structure. Nat Protoc. 2006;1(6):2876–90.

Guengerich FP. Mechanisms of cytochrome P450-catalyzed oxidations. ACS Catal. 2018;8(12):10964–76.

Hermes S, Bremm O, Garczarek F, Derrien V, Liebisch P, Loja P, et al. A time-resolved iron-specific x-ray absorption experiment yields no evidence for an Fe2+ Fe3+ transition during qa- qb electron transfer in the photosynthetic reaction center. Biochemistry. 2006;45:353–9.

Hobisch M, Holtmann D, Gomez de Santos P, Alcalde M, Hollmann F, Kara S. Recent developments in the use of peroxygenases - exploring their high potential in selective oxyfunctionalisations. Biotechnol Adv. 2021;51:107615.

Hollingsworth SA, Poulos TL. Molecular dynamics of the P450cam-PDX complex reveals complex stability and novel interface contacts. Protein Sci. 2015;24(1):49–57.

Jamaluddin M, Rao PVS, Vaidyanathan CS. Involvement of the protocatechuate pathway in the metabolism of mandelic acid. J Bacteriol. 1970;101:786–93.

Jumper J, Evans R, Pritzel A, Green T, Figurnov M, Ronneberger O, et al. Highly accurate protein structure prediction with alphafold. Nature. 2021;596(7873):583–9.

Kamimura N, Takahashi K, Mori K, Araki T, Fujita M, Higuchi Y, et al. Bacterial catabolism of lignin-derived aromatics: new findings in a recent decade: update on bacterial lignin catabolism. Environ Microbiol Rep. 2017;9(6):679–705.

Kauppi B, Lee K, Carredano E, Parales RE, Gibson DT, Eklund H, et al. Structure of an aromatic-ring-hydroxylating dioxygenase—naphthalene 1,2-dioxygenase. Structure. 1997;6: 571–86.

Kim DN, Jacobs TM, Kuhlman B. Boosting protein stability with the computational design of-sheet surfaces. Protein Sci. 2016; 25(3):702–10.

Kincannon WM, Zahn M, Clare R, Lusty Beech J, Romberg A, Larson J, et al. Biochemical and structural characterization of an aromatic ring-hydroxylating dioxygenase for terephthalic acid catabolism. Proc Natl Acad Sci U S A. 2022;119(13): e2121426119.

Kokkonen P, Beier A, Mazurenko S, Damborsky J, Bednar D, Prokop Z. Substrate inhibition by the blockage of product release and its control by tunnel engineering. RSC Chem Biol. 2021;2(2):645–55.

Kontur WS, Olmsted CN, Yusko LM, Niles AV, Walters KA, Beebe ET, et al. A heterodimeric glutathione S-transferase that stereospecifically breaks lignin's beta(R)-aryl ether bond reveals the diversity of bacterial beta-etherases. J Biol Chem. 2019; 294(6):1877–90.

Krissinel E, Henrick K. Secondary-structure matching (SSM), a new tool for fast protein structure alignment in three dimensions. Biol Crystallogr. 2004;60(12):2256–68.

Krissinel E, Henrick K. Inference of macromolecular assemblies from crystalline state. J Mol Biol. 2007;372(3):774–97.

Krissneil E, Henrick K. Detection of protein assemblies in crystals. J Mol Biol. 2005;372:164–75.

Kunzendorf A, Zirpel B, Milke L, Ley JP, Bornscheuer UT. Engineering an o-methyltransferase for the regioselective biosynthesis of hesperetin dihydrochalcone. ChemCatChem. 2023;15: e202300951.

Li Z, Jiang Y, Guengerich FP, Ma L, Li S, Zhang W. Engineering cytochrome p450 enzyme systems for biomedical and biotechnological applications. J Biol Chem. 2020;295(3):833–49.

Link TA. The structures of rieske and rieske-type proteins. Adv Inorgan Chem. 1999;47:83–157.

Lisi GP, Png CYM, Wilcox DE. Thermodynamic contributions to the stability of the insulin hexamer. Biochemistry. 2014;53(22): 3576–84.

Macheroux P. Uv-visible spectroscopy as a tool to study flavoproteins. Methods Mol Biol. 1999;131:1–7.

Mahto JK, Neetu N, Waghmode B, Kuatsjah E, Sharma M, Sircar D, et al. Molecular insights into substrate recognition and catalysis by phthalate dioxygenase from Comamonas testosteroni. J Biol Chem. 2021;297(6):101416.

Manalastas-Cantos K, Konarev PV, Hajizadeh NR, Kikhney AG, Petoukhov MV, Molodenskiy DS, et al. Atsas 3.0: expanded functionality and new tools for small-angle scattering data analysis. J Appl Cryst. 2021;54(Pt 1):343–55.

Micsonai A, Wien F, Bulyaki E, Kun J, Moussong E, Lee YH, et al. Bestsel: a web server for accurate protein secondary structure prediction and fold recognition from the circular dichroism spectra. Nucleic Acids Res. 2018;46(W1):W315–22.

Micsonai A, Wien F, Kernya L, Lee YH, Goto Y, Refregiers M, et al. Accurate secondary structure prediction and fold recognition for circular dichroism spectroscopy. Proc Natl Acad Sci U S A. 2015;112(24):E3095–103.

Morawski B, Segura A, Ornston LN. Repression of acinetobacter vanillate demethylase synthesis by VanR, a member of the GNTR family of transcriptional regulators. FEMS Microbol Lett. 2000;187(1):65–8.

Neidle EL, Hartnett C, Ornston LN, Bairoch A, Rekik M, Harayama S. Nucleotide sequences of the Acinetobacter calcoaceticus BenABC genes for benzoate 1,2 diozygenase reveal evolutionary relationships among multicomponent oxygenases. J Bacteriol. 1991;173(17):5385–95.

Noble JE. Quantification of protein concentration using UV absorbance and Coomassie dyes. Methods Enzymol. 2014;536:17–26.

Ohta T, Chakrabarty S, Lipscomb JD, Solomon EI. Near-IR MCD of the nonheme ferrous active site in naphthalene 1,2-dioxygenase: correlation to crystallography and structural insight into the mechanism of rieske dioxygenases. J Am Chem Soc. 2008;130:1601–10.

Philipp B, Kemmler D, Hellstern J, Gorny N, Caballero A, Schink B. Anaerobic degradation of protocatechuate (3,4-dihydroxybenzoate) by Thauera aromatica strain ar-1. FEMS Microbiol Lett. 2002;212:139–43.

Poulost TL, Finzelx BC, Howard AJ. High-resolution crystal structure of cytochrome P450cam. J Mol Biol. 1987;195:687–700.

Ravel B, Newville M. Athena, artemis, hephaestus: data analysis for x-ray absorption spectroscopy using IFEFFIT. J Synchrotron Radiat. 2005;12(4):537–41.

Reetz MT. Biocatalysis in organic chemistry and biotechnology: past, present, and future. J Am Chem Soc. 2013;135(34): 12480–96.

Roda S, Terholsen H, Meyer JRH, Canellas-Sole A, Guallar V, Bornscheuer U, et al. Asitedesign: a semirational algorithm for an automated enzyme design. J Phys Chem B. 2023;127(12): 2661–70.

Sarangi R, Hocking RK, Neidig ML, Benfatto M, Holman TR, Solomon EI, et al. Geometric structure determination of N694C lipoxygenase: a comparative near-edge x-ray absorption spectroscopy and extended x-ray absorption fine structure study. Inorg Chem. 2008;47(24):11543–50.

Sasoh M, Masai E, Ishibashi S, Hara H, Kamimura N, Miyauchi K, et al. Characterization of the terephthalate degradation genes of Comamonas sp. strain E6. Appl Environ Microbiol. 2006; 72(3):1825–32.

Schmitt DL, An S. Spatial organization of metabolic enzyme complexes in cells. Biochemistry. 2017;56(25):3184–96.

Serioukova IF, Li H, Zhang H, Peterson JA, Poulos T. Structure of a cytochrome P450–redox partner electron-transfer complex. Proc Natl Acad Sci U S A. 1999;96:1863–8.

Suen W-C, Gibson DT. Isolation and preliminary characterization of the subunits of the terminal component of naphthalene dioxygenase from pseudomonas putida NCIB 9816-4. J Bacteriol. 1993;175:5877–81.

Svergun D. Determination of the regularization parameter in indirect-transform methods using perceptual criteria. J Appl Cryst. 1992;25(4):495–503.

Swoboda BEP. The relationship between molecular conformation and the binding of flavin-adenine dinucleotide in glucose oxidase. Biochim Biophys Acta. 1969;175:365–79.

Takahashi K, Kamimura N, Hishiyama S, Hara H, Kasai D, Katayama Y, et al. Characterization of the catabolic pathway for a phenylcoumaran-type lignin-derived biaryl in Sphingobium sp. strain SYK-6. Biodegradation. 2014;25(5):735–45.

Takahashi K, Miyake K, Hishiyama S, Kamimura N, Masai E. Two novel decarboxylase genes play a key role in the stereospecific catabolism of dehydrodiconiferyl alcohol in Sphingobium sp. strain SYK-6. Environ Microbiol. 2018;20(5):1739–50.

Tavakoli A, Hamzah A, Rabu A. Expression, purification and kinetic characterization of recombinant benzoate dioxygenase from Rhodococcus ruber UKMP-5M. Mol Biol Res Commun. 2016;5(3):133–42.

Tournier V, Topham CM, Gilles A, David B, Folgoas C, Moya-Leclair E, et al. An engineered PET depolymerase to break down and recycle plastic bottles. Nature. 2020;580(7802): 216–9.

Tripathi S, Li H, Poulos TL. Structural basis for effector control and redox partner recognition in cytochrome P450. Science. 2013; 340:1227–9.

Tsai P-C, Chakraborty J, Suzuki-Minakuchi C, Terada T, Kotake T, Matsuzawa J, et al. The a- and b-subunit boundary at the stem of the mushroomlike a3b3-type oxygenase component of rieske non-heme iron oxygenases is the rieske-type ferredoxin-binding site. Appl Environ Microbiol. 2022;88(15):e0083522.

Tsang HT, Batie CJ, Ballou DP, Penner-Hahn JE. X-ray absorption spectroscopy of the [2-iron-2-sulfur] rieske cluster in pseudomonas cepacia phthalate dioxygenase. Determination of core dimensions and iron ligation. Biochemistry. 1989;28(18): 7233–40.

Tsang H-T, Batie CJ, Ballou DP, Penner-Hahn JE. Structural characterization of the mononuclear iron site in pseudomonas cepacia phthalate DB01 dioxygenase using x-ray absorption spectroscopy. J Biol Inorg Chem. 1996;1:24–33.

Varadi M, Anyango S, Deshpande M, Nair S, Natassia C, Yordanova G, et al. Alphafold protein structure database: massively expanding the structural coverage of protein-sequence space with high-accuracy models. Nucleic Acids Res. 2022; 50(D1):D439–44.

Walsh T, Ballou D. Halogenated protocatechuates as substrates for protocatechuate dioxygenase from pseudomonas cepacia. J Biol Chem. 1982;41(4):1291.

Webb SM. Sixpack: a graphical user interface for xas analysis using IFEFFIT. Phys Script. 2005;T115:1011–4.

Wei R, Oeser T, Zimmermann W. Synthetic polyester-hydrolyzing enzymes from thermophilic actinomycetes. Adv Appl Microbiol. 2014;89:267–305.

Wolfe MD, Altier DJ, Stubna A, Popescu CV, Munck E, Lipscomb JD. Benzoate 1,2-dioxygenase from pseudomonas putida: single turnover kinetics and regulation of a two-component Rieske dioxygenase†. Biochemistry. 2002;41: 9611–26.

Wolfe MD, Lipscomb JD. Hydrogen peroxide-coupled cis-diol formation catalyzed by naphthalene 1,2-dioxygenase. J Biol Chem. 2003;278(2):829–35.

Wood EJ. Data for biochemical research. Oxford Science Publications. Biochem Edu. 1987;15(2):103-125.

Yoshida S, Hiraga K, Takehana T, Taniguchi I, Yamaji H, Maeda Y, et al. A bacterium that degrades and assimilates poly(ethylene terephthalate). Science. 2016;351(6278):1196–9.

Yun SH, Yun CY, Kim SI. Characterization of protocatechuate 4,5-dioxygenase induced from p-hydroxybenzoate-cultured pseudomonas sp k82. J Microbol. 2004;42(2):152–5.

Zhang JE, Maggiolo AO, Alfonzo E, Mao RZ, Porter NJ, Abney NM, et al. Chemodivergent C(sp(3))-H and C(sp(2))-H cyanomethylation using engineered carbene transferases. Nat Catal. 2023;6(2):152–60.

SUPPORTING INFORMATION

Additional supporting information can be found online in the Supporting Information section at the end of this article.